0D Bi nanodots/2D Bi$_3$NbO$_7$ nanosheets heterojunctions for efficient visible light photocatalytic degradation of antibiotics: Enhanced molecular oxygen activation and mechanism insight

Kai Wang, Yuan Li, Gaoke Zhang*, Jun Li, Xiaoyong Wu

State Key Laboratory of Silicate Materials for Architectures, Hubei Key Laboratory of Mineral Resources Processing and Environment, Hubei Provincial Collaborative Innovation Center for High Efficient Utilization of Vanadium Resources, School of Resources and Environmental Engineering, Wuhan University of Technology, 122 Luoshi Road, Wuhan 430070, China

ARTICLE INFO

ABSTRACT

Solar-driven molecular oxygen activation is a promising and low energy-cost way for environmental remediation. To fabricate semimetal/semiconductor composite photocatalyst is an effective strategy to accelerate the transfer and separation of photogenerated carriers for boosting molecular oxygen activation. Herein, we report a 0D Bi nanodots/2D Bi$_3$NbO$_7$ nanosheets heterostructured composite with enhanced molecular oxygen activation under visible light irradiation, which was synthesized by a two-step wet chemical method. Transmission electron microscopy (TEM) analysis shows that the Bi nanodots with diameters of 2–5 nm were uniformly distributed on the surface of Bi$_3$NbO$_7$ nanosheets. More importantly, both experiments and density functional theory (DFT) calculations confirm that a strong covalent interaction existed between the Bi atom of Bi nanodots and Bi–O layer on the surface of the Bi$_3$NbO$_7$ nanosheets, which enhanced the visible light absorbability of the composite, fostered the transfer and separation of its interfacial photogenerated carriers, and promoted the activation of molecular oxygen into superoxide radicals ($\cdot$O$_2^-$) and singlet oxygen (^{1}O$_2$) by the composite under visible light illumination for degradation of ciprofloxacin (CIP). The photocatalytic degradation rate of CIP by the Bi/Bi$_3$NbO$_7$ composites is 4.58 times higher than that by the pristine Bi$_3$NbO$_7$. The Bi/Bi$_3$NbO$_7$ photocatalyst still revealed high photocatalytic activity even after five cycles. This work elucidates the mechanism of molecular oxygen activation over 0D/2D semimetal-semiconductor system and provides a promising approach for designing high efficient 0D/2D photocatalysts toward sustainable environmental remediation.

1. Introduction

In the past decades, the abuse of antibiotics causes great concerns on natural water bodies and human health. Nowadays, semiconductor photocatalysis has been regarded as a promising approach to decompose the excess antibiotics in environmental water bodies [1–3]. It is well known that activation of molecular oxygen process acts an important role in photocatalytic degradation of antibiotics. The effective capture of molecular oxygen is capable of suppressing the recombination of photo-induced electron-hole pairs and generates reactive oxygen species (ROS), such as superoxide ($\cdot$O$_2^-$), singlet oxygen (^{1}O$_2$), hydroxyl ($\cdot$OH), which are crucial active sources of photocatalytic antibiotics degradation [4–6]. Thus, the construction of novel visible-light responsive photocatalysts based molecular oxygen activation for effectively antibiotics degradation still remains a huge challenge.

Bismuth-based photocatalysts have triggered widespread concerns for their high charge separation efficiency and efficient utilization of solar spectrum [7–11]. Typically, on account of the unique layered structure, suitable band gap (2.5–2.75 eV) and high photochemical stability, bismuth niobates (Bi$_3$NbO$_7$) has been regarded as a promising semiconductor photocatalyst for environmental pollutants removal and antibiotics degradation [12–14]. Our group and Hu et al. had reported Bi$_3$NbO$_7$ nanoparticles and porous Bi$_3$NbO$_7$ nanosheets, which showed good adsorption ability and visible light photocatalytic performance [15,16]. However, the photocatalytic performance of Bi$_3$NbO$_7$ is markedly restricted by the insufficient of solar spectrum absorption and poor molecular oxygen activation efficiency. Element doping and heterojunctions construction are effective strategies to improve the photocatalytic acticity of this semiconductor photocatalyst system [17,18]. In addition, low dimension metal nanoparticles deposition on semiconductor nanostructure is a meaningful method to extend the visible light responsive range and the molecular oxygen activation efficiency of

---

* Corresponding author.
  E-mail address: gkzhang@whut.edu.cn (G. Zhang).

Bi_3NbO_7.

Noble metal nanoparticles such as Ag, Au and Pt modified semiconductors have been widely applied to accelerate the solar spectrum absorption and photocatalytic activity of photocatalysts. The semimetal Bi, as a direct plasmonic photocatalyst, has been confirmed to exhibit stable photocatalytic performance due to the SPR property, similar to many noble metal nanoparticles [19–23]. However, the photocatalytic efficiency of single semimetal Bi photocatalyst calls for further improvements in photochemical filed. The zero-dimension Bi nanodots deposed on the surface of semiconductor photocatalysts could boost the interfacial charge flow by constructing Schottky barriers at the interface of the metal/catalyst systems and play as an electron trap to separate photoinduced carriers [24–27]. Recently, deposition of Bi nanoparticles onto semiconductor photocatalysts, such as TiO_2, BiOI, BiOCl, Bi_2WO_6, and CdS displayed high photocatalytic activities for the environmental pollutants removal and hydrogen evolution [28–35]. It might be a fantasy approach to boost the photocatalytic performance and molecular oxygen activation of the Bi_3NbO_7 by constructing 0D Bi nanodots/2D Bi_3NbO_7 nanosheets heterojunction system.

In the present report, we successfully fabricated 0D/2D Bi/Bi_3NbO_7 heterojunction photocatalysts, which displayed superior molecular oxygen activation ability for photocatalytic antibiotics degradation. Subsequently, the semimetal Bi/Bi_3NbO_7 homogeneous junction and charge difference distribution between Bi_3NbO_7 and Bi were calculated by theoretical calculations and the 0D Bi nanodots decorated Bi_3NbO_7 nanosheets exhibited remarkably enhanced photocatalytic performance for ciprofloxacin (CIP) degradation. Furthermore, PL, time-resolved transient PL decay spectra, and photo-electrochemistry analysis were used to analyze the interfacial charge separation of Bi/Bi_3NbO_7. Consequently, this work could provide enlightenment for synthesizing 0D/2D Bi-based photocatalysts with high photocatalytic performance.

2. Experimental

2.1. Synthesis

Bi_3NbO_7 nanosheets were synthesized by a facile hydrothermal method. 1.455 g of $Bi(NO_3)_3 \cdot 5H_2O$ was dissolved into 10 mL glacial acetic acid as solution A and 0.538 g of $C_{10}H_5NbO_{20}$ was added into 40 mL methanol as solution B. Subsequently, solution A was slowly added into as solution B under vigorous stirring followed by 30 mL benzyl alcohol after 30 min. The pH value of suspension was adjusted to 13.2 using KOH solution. The suspension was transferred to PPL-lined autoclave and heated at 180 °C for 24 h. The yellow products were washed with ethanol for five times and dried at 80 °C for 4 h. Bi/Bi_3NbO_7 nanocomposites were fabricated by a facile solvothermal method. (0.005, 0.02, 0.035, 0.05) mmol $Bi(NO_3)_3 \cdot 5H_2O$ was dissolved in 65 mL ethylene glycol (EG) for 30 min. Then 0.42 g Bi_3NbO_7 powder was added into the above solution under ultrasonic dispersion for 2 h and heated at 180 °C for 8 h. The obtained composites were washed with ethanol for five times and dried at 80 °C for 12 h. The contents of Bi in Bi/Bi_3NbO_7 composites were 1, 4, 7, and 10% by mass ratio.

2.2. Characterization

The morphologies and high angle angular dark field-scanning transmission electron microscopy (HAADF-STEM) images of the sample were examined by transmission electron microscopy (Talos F200S, Thermo Fisher). The specific surface areas of the samples were tested by Micromeritics ASAP 2020. The absorption edges of samples were tested by a UV–vis spectrophotometer (Lambda 750S). The crystallinity of samples was analyzed by X-ray diffraction (XRD) on a X'Pert PRO diffractometer with Cu Kα radiation. X-ray photoelectron spectra (Thermo Fisher Multi-lab 2000) were tested on a monochromatic Al Kα source and the C(1s) binding energy is 284.6 eV. Photoluminescence spectra were recorded by fluorescence spectrophotometer (Shimadzu RF-5301)

and the Time-resolved transient PL decay was tested by Edinburgh FLSP920 with an excitation wavelength of 312 nm. The EPR (electron paramagnetic resonance) spectra were recorded on a Bruker A-300 spectrometer. Electrochemical impedance spectroscopy and transient photocurrent were analyzed by an electrochemical workstation (chi660E) in the electrolyte was 0.5 M Na_2SO_4.

2.3. Photocatalytic activity and molecular oxygen activation

The photocatalytic performance of the Bi/Bi_3NbO_7 catalysts were measured by the degradation of CIP, using 300 W Xe lamp as light source with 400 nm cutoff filter. Typically, 50 mg photocatalysts was placed in 100 mL CIP solution (10 mg/L). The concentration of CIP in aqueous solution was analyzed by UV–vis spectrophotometer (Thermo Orion AquaMate 8000) at wavelength of 277 nm. Total organic carbon (TOC) was analysed by total organic carbon analyzer (Elementar, Germany). Determination of the intermediates of CIP was carried out on a LC–MS system (Agilent Quadrupole 6120).

The ESR experiments were tested by electron paramagnetic resonance spectrometer (Bruker, A-300). Typically, 20 mg catalysts were dispersed in 1 mL of water or methanol, and 45 μL of 5,5-Dimethyl-1-pyrroline-N-oxide (DMPO) was added before visible light irradiation. 2,2,6,6-tetramethylpiperidine (TEMP) was used to detect the singlet oxygen ($^1O_2$). The 20 μM of nitroblue tetrazolium (NBT) was applied to quantize the amount of $\cdot O_2^-$, which was quantitatively analyzed by measuring the dissipation of NBT on a UV–vis spectrophotometer at 259 nm.

2.4. Computational details

Vienna ab initio simulation package (VASP) based on density functional theory (DFT) was used to calculate the electronic structure of Bi_3NbO_7 and Bi/Bi_3NbO_7. The exchange-correction function was measured by the Perdew-Burke-Ernzerhof (PBE) formulation of the generalized gradient approximation (GGA). The cutoff energy of atomic wave functions was 400 eV and the k-meshes $3 \times 2 \times 2$ and $3 \times 2 \times 4$ are performed in the calculations of Bi_3NbO_7 and Bi/Bi_3NbO_7, respectively. During the optimizations, the energy and force converged to 10^{-5} eV/atom and 0.01 eV/Å, respectively. Then 8 Bi atoms were supported on the surface of Bi_3NbO_7.

3. Results and discussion

As shown in Fig. 1, the diffraction peaks of the Bi_3NbO_7 at 2θ degree of 28.19°, 32.66°, 46.86°, 55.59° have been observed, which matched

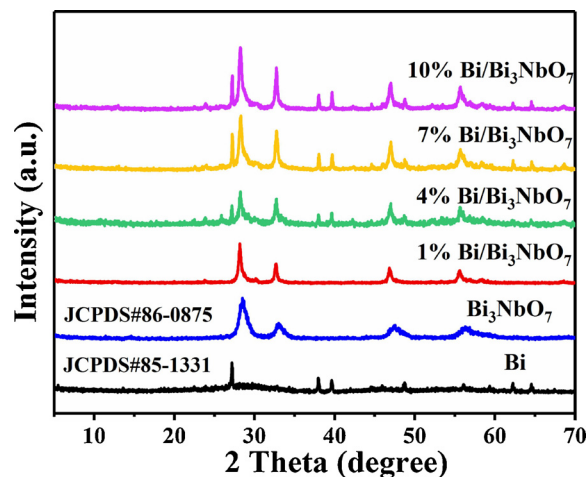**Fig. 1.** XRD patterns of the pure Bi_3NbO_7, Bi and X% Bi/Bi_3NbO_7 (X = 1, 4, 7, 10).

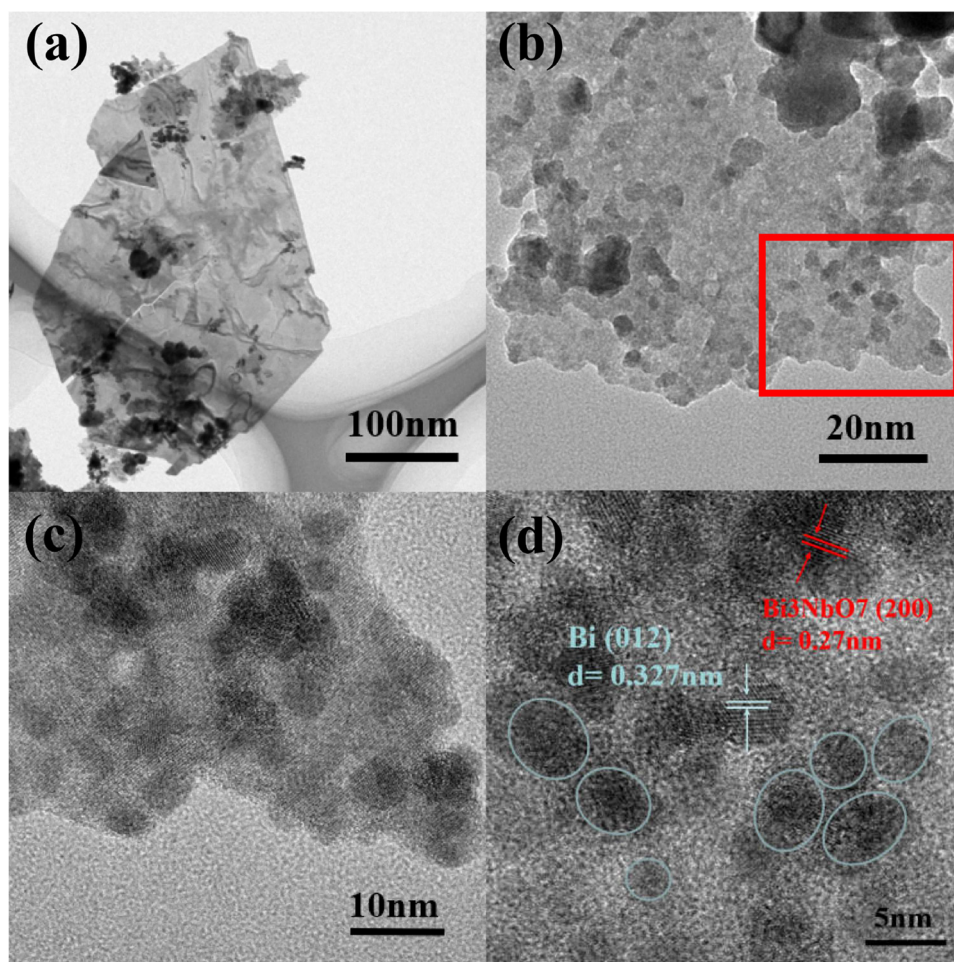**Fig. 2.** TEM images of (a) Bi_3NbO_7, (b and c) 7% Bi/Bi_3NbO_7. HRTEM image of (d) 7% Bi/Bi_3NbO_7.

well with the (111), (200), (220), (311) planes of the cubic Bi_3NbO_7 (JCPDS, No. 86-0875) [16]. For the X% Bi/Bi_3NbO_7 (X = 4, 7, and 10) composites, all the peaks of Bi_3NbO_7 were clearly observed at Bi/ Bi_3NbO_7 composites, which forecast that the introduction of Bi has no influence to the crystalline structure of Bi_3NbO_7. Meanwhile, the minor peaks at 27.27°, 38.13°, 39.74°, 48.86° were founded, which can be assigned to (012), (104), (110), (202) planes of metallic Bi (JCPDS, No. 85-1331) [33]. Remarkably, no obvious diffraction peaks for Bi could be observed in the pattern of 1% Bi/Bi_3NbO_7, which might be resulted from the infinitesimal Bi nanoparticles in 1% Bi/Bi_3NbO_7 samples.

The morphologies of the Bi_3NbO_7 and Bi/Bi_3NbO_7 composites were investigated by SEM and TEM. Fig. S1 can lead to the fact that the pure Bi_3NbO_7 displays 2D structure [16]. More detailed informations of the Bi_3NbO_7 and Bi/Bi_3NbO_7 samples could be observed from TEM images. From Fig. 2a, the TEM image of Bi_3NbO_7 is in good agreement with the sheet-like structure in the SEM image and the thickness is quite thin. Fig. 2b and c indicates that Bi nanodots are well dispersed on the surface of Bi_3NbO_7 nanosheet with diameters is 2–5 nm. The uniformly loaded Bi nanodots were beneficial to the interfacial charge flow from Bi_3NbO_7 nanosheet to Bi nanodots. It can be clear observed in Fig. 2d that the lattice fringes with spacing of 0.326 nm is consistent with the (012) crystal planes of semimetal Bi (JCPDS, No. 85-1331) [31]. HAADF-STEM image and corresponding EDX mappings of 7% Bi/Bi_3NbO_7 was used to inspect the elemental composition and distribution (Fig. S2). The mapping images display a homogeneous distribution of Bi, Nb, and O elements in 7% Bi/Bi_3NbO_7.

The FTIR spectra of the Bi_3NbO_7 and Bi/Bi_3NbO_7 composites were exhibited in Fig. 3. As shown in the spectrum of Bi_3NbO_7, the broad
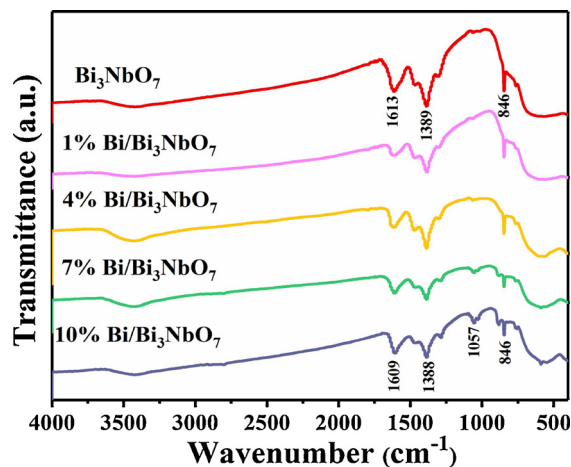

Fig. 3. FT-IR spectra of the Bi_3NbO_7 and X% Bi/Bi_3NbO_7 (X = 1, 4, 7, 10).

bands ranges from 600–1200 cm^{-1} are attributes to Nb−O, Nb−O−Nb and Bi−O stretching vibrations and the band at 1613 cm^{-1} could correspond to the water molecules adsorbed on the surface of the Bi_3NbO_7 [31]. The weakened peak at 1388 cm^{-1} and a new peak appeared at 1057 cm^{-1} demonstrates the presence of metallic Bi on the Bi/Bi_3NbO_7 composites. The FTIR results declare that the structure of Bi_3NbO_7 does not change with the introduction of semimetal Bi, which is in consensus with the XRD analysis.

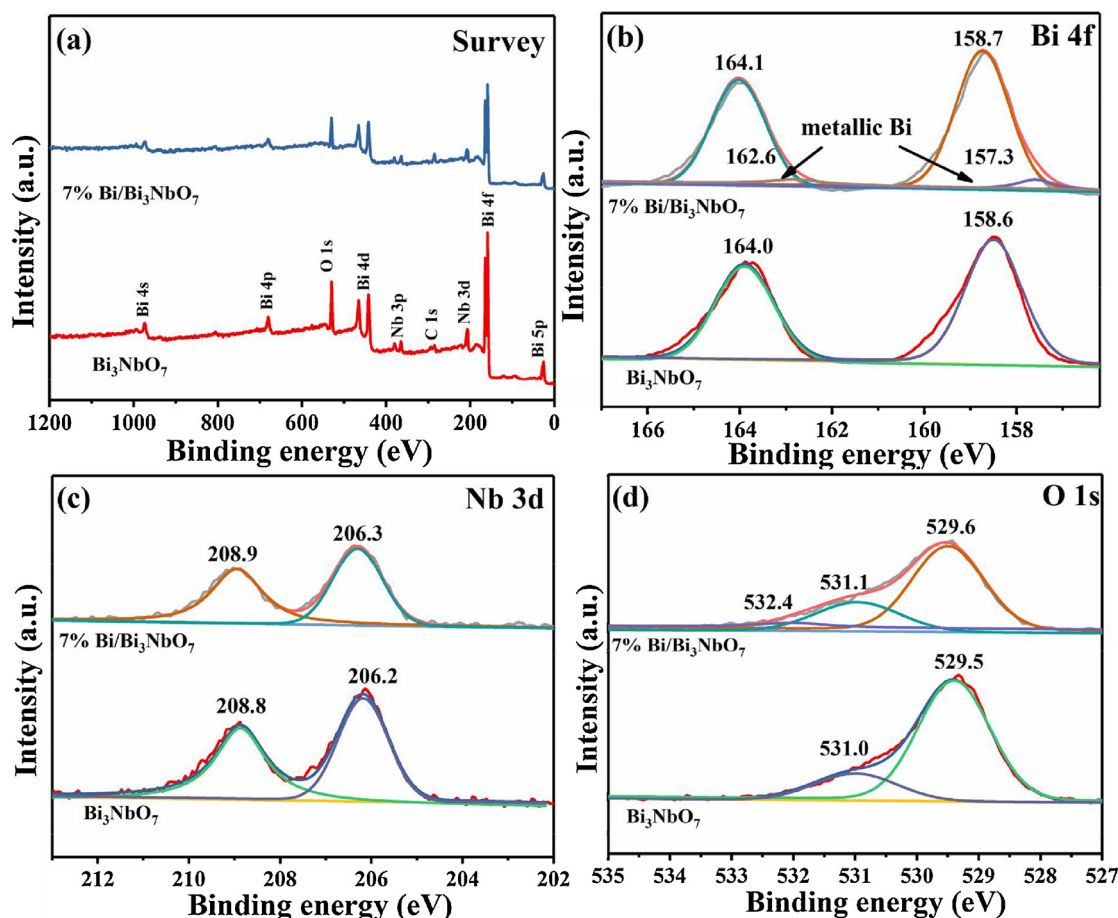XPS was further measured to investigate the surface chemical states

Fig. 4. XPS spectra of the Bi_3NbO_7 and 7% Bi/Bi_3NbO_7 composites. (a) the survey scan, (b) Bi 4f, (c) Nb 3d, and (d) O 1s.

of Bi/Bi_3NbO_7 composite. As shown in Fig. 4a, the survey spectrum illustrates that composition of the Bi_3NbO_7 and 7% Bi/Bi_3NbO_7 composites included Bi, Nb and O. Fig. 4b displays Bi 4f spectra in the 7% Bi/Bi_3NbO_7 and Bi_3NbO_7 sample. It can be observed that two peaks at 164.0 and 158.6 eV are referred to the binding energies of Bi $4f_{5/2}$ and Bi $4f_{7/2}$, respectively, which are the characteristics of Bi^{3+} in Bi_3NbO_7. The Bi 4f peaks in 7% Bi/Bi_3NbO_7 can be divided into four peaks at 158.7, 164.1 eV, and 157.3, 162.6 eV, respectively. Those peaks located at 157.3 and 162.6 eV in the XPS spectrum of 7% Bi/Bi_3NbO_7 can be attributed to semimetal Bi nanodots on the surface of Bi_3NbO_7 nanosheets, which is consistent with the results of HRTEM analysis (Fig. 2d) [24]. The binding energy at 206.2 and 208.8 eV are assigned to Nb $3d_{3/2}$ and Nb $3d_{5/2}$ peaks, respectively (Fig. 4c), which are well matched with the Nb^{5+} in Bi_3NbO_7 and 7% Bi/Bi_3NbO_7 composites [16]. When semimetal Bi was introduced, the two peaks of Nb^{5+} shifted to 208.9 and 206.3 eV in 7% Bi/Bi_3NbO_7 composites, respectively. As shown in Fig. 4d, the O 1s spectrum of Bi_3NbO_7 can be divided into two peaks and the peak located at 529.5, and 531.0 eV could be assigned to Bi–O bond and Nb–O bond of Bi_3NbO_7 crystal structures, respectively [31]. Interestingly, a new peak at around 532.4 eV in the O 1s spectrum is observed for the 7% Bi/Bi_3NbO_7 composites, which can be ascribed to oxygen in hydrated species OH on the surface [33]. Meanwhile, the XPS of Bi_3NbO_7 composites before and after solvothermal reaction were also analyzed. As shown in Fig. S3a–c, the high-resolution spectra of Bi 4f, Nb 3d and O 1s changed little and overlapped basically, which indicated that the second solvothermal process by adding ethylene glycol as reducing agent had little influence on the physicochemical property of Bi_3NbO_7. Furthermore, the EPR spectra of Bi_3NbO_7 before and after solvothermal reaction in Fig. S3d exhibited that there is no obvious peak of oxygen vacancy after solvothermal reaction. These results

illustrated the existence of 0D Bi nanodots reduced by Bi^{3+} of adding Bi $(NO_3)_3 \cdot 5H_2O$ in second solvothermal process, further indicating the formation of Bi/Bi_3NbO_7 heterostructure.

UV–vis absorption spectra of pristine Bi_3NbO_7 and Bi/Bi_3NbO_7 composites were exhibited in Fig. 5. From Fig. 5a, the absorption edge of pristine Bi_3NbO_7 is approximately located at 462 nm. The absorption edges of the Bi/Bi_3NbO_7 composites exhibited a prominent redshift, which confirmed that the Bi/Bi_3NbO_7 composites further enhanced the visible light absorption [34]. As shown inset of Fig. 5a, the optical absorption of the obtained samples changed with increasing the Bi content in the samples, which is consistent with their color changes from light yellow to grey. Notably, a typical SPR absorption region of semimetal Bi at about 500 nm can be observed in Fig. 5a. According to the previous literature, the enhanced visible light absorption ranges from 450 to 600 nm can be easily detected from the SPR effects of semimetal Bi [26]. Instead, the Bi/Bi_3NbO_7 composites almost absorb full region of light, exhibits especially enhanced absorption in the visible light range (450–700 nm), which can be directly ascribed to SPR absorption from 0D Bi nanodots [23]. Fig. 5b indicates that the band gap (Eg) of the sample is located at 2.69 eV for Bi_3NbO_7. In general, the 0D Bi nanodots deposed on Bi_3NbO_7 can enhance the visible light absorption and molecular oxygen activation of pristine Bi_3NbO_7.

Additionally, density functional theory (DFT) was applied to explore the electron properties of Bi_3NbO_7 and Bi/Bi_3NbO_7 composites theoretically. The cell models of Bi_3NbO_7 and Bi/Bi_3NbO_7 were shown in Fig. 6a, respectively. As shown in Fig. 6b, the upper valence band is the hybridization of Bi 6s, Nb 4d and O 2p orbitals, respectively [36–38] and the conduction band from 2.6 to 10.9 eV is mostly contributed by the hybridization of Bi 5d, Nb 4d and O 2p orbital. The calculated band gap value of Bi_3NbO_7 (2.56 eV) tends to be smaller than the

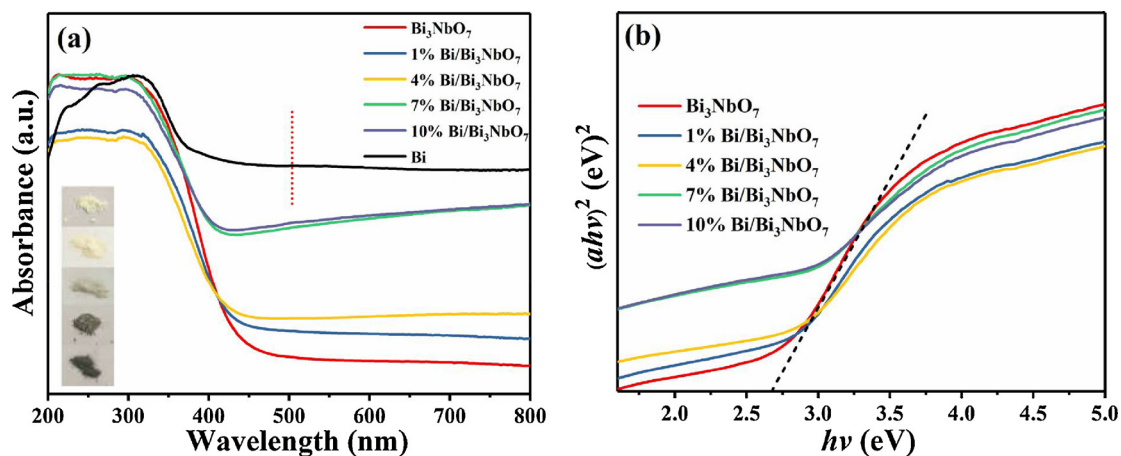**Fig. 5.** (a) UV–vis diffuse reflectance spectra and (b) Plots of $(\alpha h v)^2$ versus hv for of the Bi_3NbO_7 and serial Bi/Bi_3NbO_7 composites.

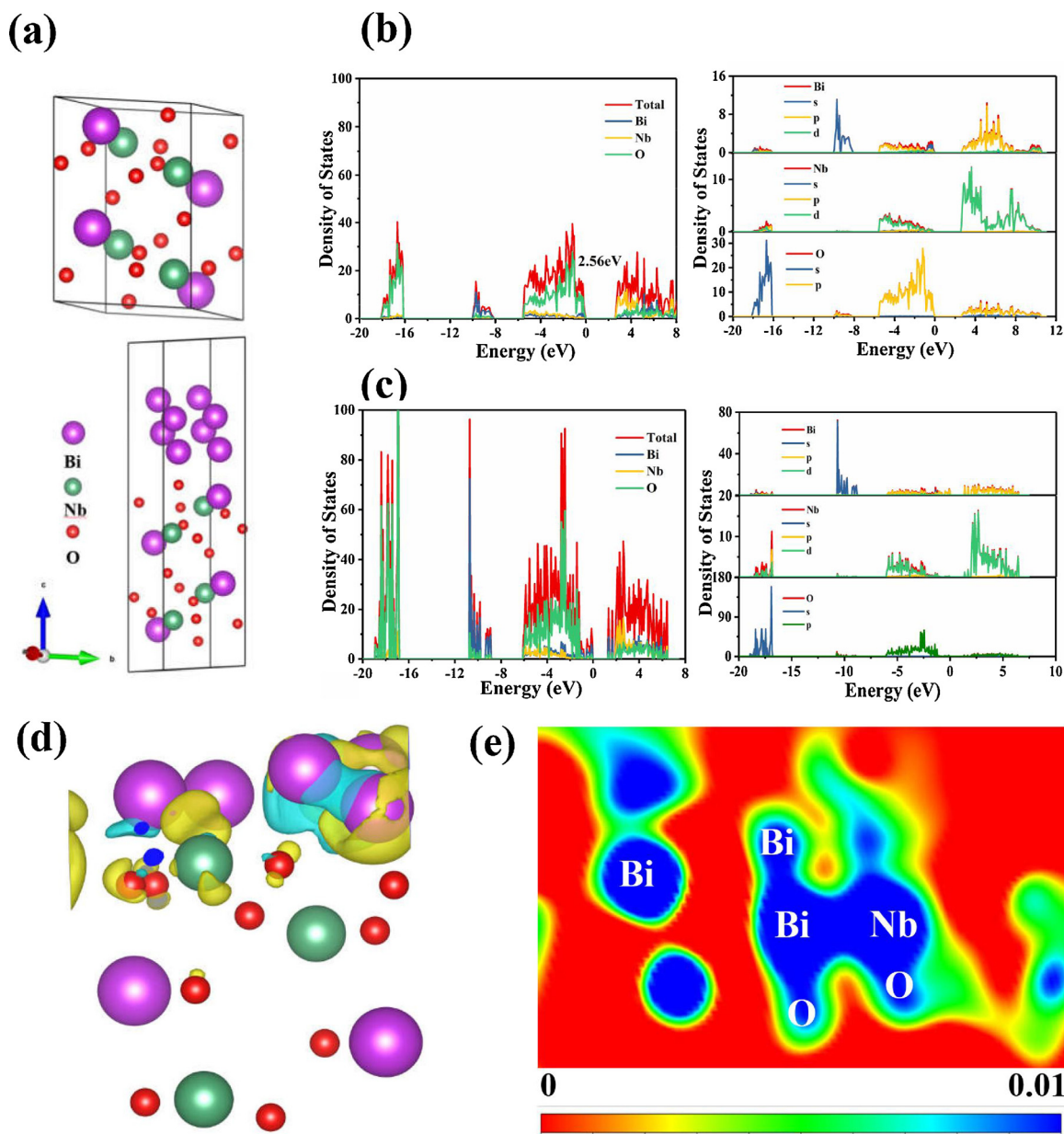**Fig. 6.** (a) Optimized geometric structures of Bi_3NbO_7 and Bi/Bi_3NbO_7 nanocomposite. The TDOS and corresponding PDOS of (b) Bi_3NbO_7 and (c) Bi/Bi_3NbO_7 nanocomposite. (d) Charge difference distribution and (e) electronic location function (ELF) of Bi/Bi_3NbO_7.

experimental value (2.69 eV), owing to the restriction of the DFT calculation. Meanwhile, we calculate the density of state (DOS) of Bi/Bi$_3$NbO$_7$ [39]. In comparison with the DOS for perfect Bi$_3$NbO$_7$, the density of states at valence band maximum (VBM) of Bi/Bi$_3$NbO$_7$ was significantly increased by the contribution of the orbital from Bi element. The conduction band of Bi/Bi$_3$NbO$_7$ shifted to lower energy levels, which is beneficial to promote the generation of photogenerated charge carriers [26,40]. Fig. 6d displays the charge difference distribution of Bi atom layer on Bi$_3$NbO$_7$ unit cell. It's obvious that the Bi−O layer of Bi$_3$NbO$_7$ donates abundant free electrons to metal Bi atom. From Fig. 6e, the electronic location function (ELF) demonstrates the existence of a strong covalent interaction between the Bi atom of Bi nanodots and Bi−O layer on the surface of the Bi$_3$NbO$_7$ nanosheets, forming a charge transfer channel to transfer from Bi$_3$NbO$_7$ to metal Bi nanodots [40]. To confirm the effect of Bi nanodots on the molecular oxygen activation, the charge distributions of Bi$_3$NbO$_7$ and Bi/Bi$_3$NbO$_7$ with O$_2$ adsorption were also calculated as presented in Fig. S4. When Bi atom is introduced, the charge distribution between the O$_2$ molecules and Bi layer displays a typical funnel-like three-dimensional structure, which indicated the outermost electrons tend to accumulate on oxygen molecules adsorbed on the surface of Bi layer of Bi/Bi$_3$NbO$_7$, which attributes to the activation of O$_2$ into •O$_2^-$.

The photocatalytic activities of Bi$_3$NbO$_7$ and serial Bi/Bi$_3$NbO$_7$ composites were evaluated by the degradation of typical antibiotics ciprofloxacin (CIP). Only 4% CIP in the solution were degraded within 120 min under visible light irradiation in the absence of catalyst. As shown in Fig. 7a, it is obvious that 36, 51, 64, 86, and 74% of CIP were decomposed by Bi$_3$NbO$_7$ and serial Bi/Bi$_3$NbO$_7$ composites with different content of Bi nanodots, respectively. Notably, the 7% Bi/Bi$_3$NbO$_7$ composite exhibited the highest photocatalytic performance. From Fig. S5, the peak at 277 nm (maximum absorption wavelength of CIP) was rapidly weakened, reflecting that the CIP molecular was decomposed by the reactive oxygen species generated by Bi$_3$NbO$_7$ photocatalysts. The corresponding degradation rate constants (min^{-1}) of CIP were also presented in Fig. 7b, and obviously, the 7% Bi/Bi$_3$NbO$_7$ exhibited the highest rate (0.01427) in CIP degradation progress, which is about 4.58 times higher than that of pure Bi$_3$NbO$_7$. TOC removal was chosen as a mineralization index to analyse the CIP degradation progress. As shown in Fig. 7c, the 7% Bi/Bi$_3$NbO$_7$ samples get a total TOC removal efficiency of 53% after 180 min, which is higher than that of pure Bi$_3$NbO$_7$ (19%) under same conditions, indicating that the Bi/Bi$_3$NbO$_7$ composites present enhanced mineralization ability in antibiotics degradation process. For comparison, photocatalytic CIP degradation with commercial TiO$_2$ (P25), pure Bi$_3$NbO$_7$, and Bi was also measured with the same conditions under the visible light irradiation, respectively. As shown in Fig. 7d, the 7% Bi/Bi$_3$NbO$_7$ composite exhibited the higher-up photocatalytic performance over pure Bi$_3$NbO$_7$, semimetal Bi, and P25, confirming that constructing strong coupled 0D/2D structure significantly improved the photocatalytic activities.

In this study, the degradation intermediates of CIP during the photocatalytic process were detected by LC–MS. LC–MS chromatogram and *m/z* of degraded products are listed in Fig. S6. By referencing relevant reports, the possible photocatalytic degradation pathways of CIP are displayed in Scheme 1. Three major degradation pathways are
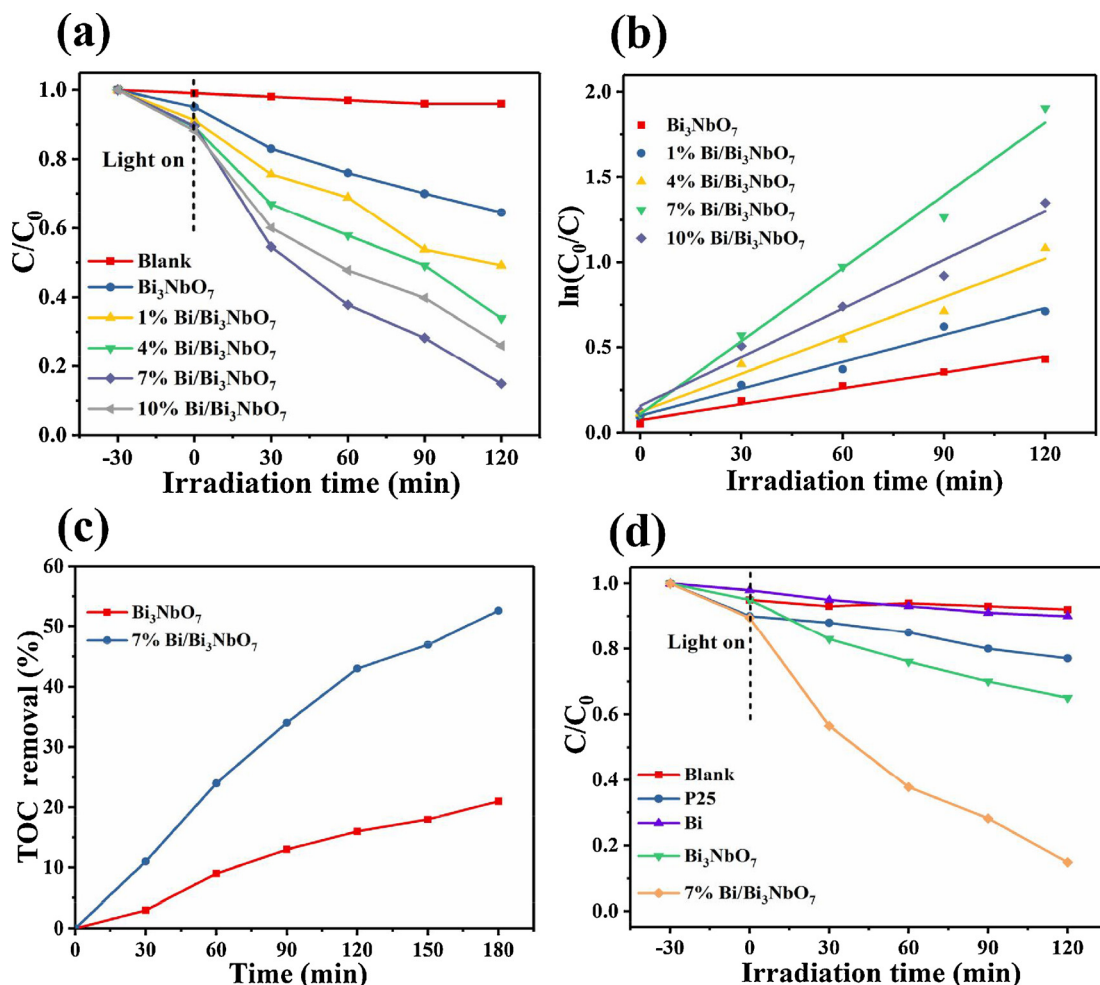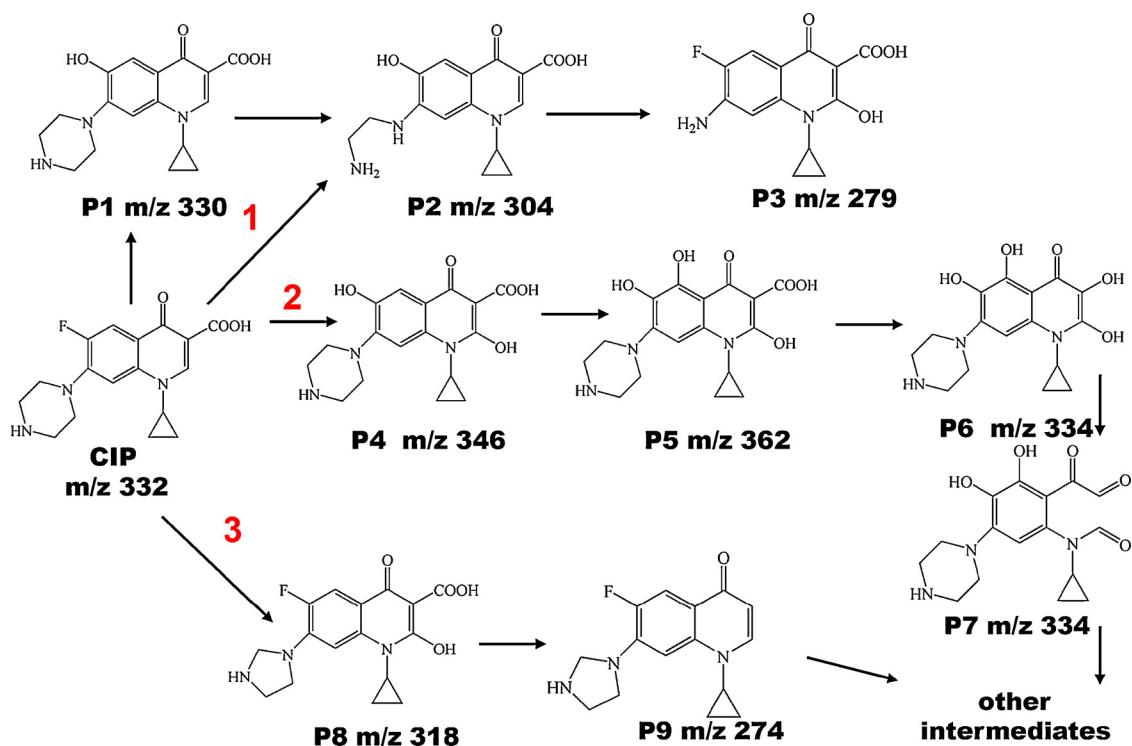

Fig. 7. (a) Photocatalytic degradation curves of CIP solution and (b) first-order rate constants of CIP degradation by series of Bi/Bi$_3$NbO$_7$ composites. (c) TOC removal curves of Bi$_3$NbO$_7$ and 7% Bi/Bi$_3$NbO$_7$ photocatalysts and (d) photocatalytic degradation curves of CIP by different catalysts.

**Scheme 1.** Possible photocatalytic degradation pathways of CIP.

presented. Pathway 1 : CIP → P1 (m/z = 330) → P2 (m/z = 304) → P3 (m/z = 279). In this degradation process, the cleavage of the piperazine ring mainly took place. Pathway 2 : CIP → P4 (m/z = 346) → P5 (m/z = 362) → P6 (m/z = 334) → P7 (m/z = 334). This pathway was mainly a hydroxylation process. CIP was subjected to varying degrees of hydrolysis and generated P4, P5, and P6. Then the quinolone ring was broken, resulting in the formation of P7. Pathway 2 : CIP → P4 (m/z = 346) → P5 (m/z = 362) → P6 (m/z = 334) → P7 (m/z = 334). Pathway 3 : CIP → P8 (m/z = 318) → P9 (m/z = 274). The formation of P8 (m/z = 318) with a five-membered ring structure in piperazine ring moiety during CIP degradation was proposed. Comparing with P8, the molecular weight of intermediate P9 was decreased by 44, just corresponding to one molecule of CO_2 [41–43]. Both pathways would finally mineralize CIP into CO_2 and H_2O, as well as inorganic oxidized N and F [41].

The photocatalytic stability of Bi/Bi$_3$NbO$_7$ composites was also evaluated by the degradation of CIP solution (Fig. 8). The 7% Bi/Bi$_3$NbO$_7$ composite was still maintained at 82% after five cycles, which indicates that the Bi/Bi$_3$NbO$_7$ composites are a stable catalyst for the photocatalytic antibiotics degradation. Moreover, the XRD and FT-IR patterns of the 7% Bi/Bi$_3$NbO$_7$ composite before and after

photocatalytic experiments were also analyzed as shown in Fig. 8b and c. It was obvious that the XRD and FT-IR patterns of the 7% Bi/Bi$_3$NbO$_7$ composite after five times had almost no prominent decrease compared with the fresh one.

Radical species trapping experiments were measured to detect the generated reactive oxygen species in photocatalytic CIP degradation. Benzoquinone, Carotene, Sodium oxalate and Isopropanol were used as •O_2^-, $^1O_2$, h$^+$ and •OH scavengers, respectively [4]. From Fig. 9a, the CIP degradation rates of Bi$_3$NbO$_7$ were dropped to 29%, 27%, 13%, 15%, 25%, and 36% in the presence of Benzoquinone, Carotene, Sodium oxalate, Isopropanol, N_2 bubbling and without scavengers respectively, confirming that •O_2^- and $^1O_2$ plays no essential contribution in CIP degradation. However, the CIP degradation rates of 7% Bi/Bi$_3$NbO$_7$ degraded slowly in the presence of Benzoquinone, Carotene, N_2 bubbling and Isopropanol, confirming that •O_2^- and $^1O_2$ together acted the important role in the antibiotics degradation (Fig. 9b) and •OH contributes some in degradation process. Furthermore, electron spin resonance (ESR) were used to further investigate the existence of reactive oxygen species [32]. Fig. 9c shows the ESR signals of DMPO-•O_2^- for Bi$_3$NbO$_7$ in dark and Bi$_3$NbO$_7$, 7% Bi/Bi$_3$NbO$_7$ composite under visible light irradiation. It is obvious that the 7% Bi/Bi$_3$NbO$_7$
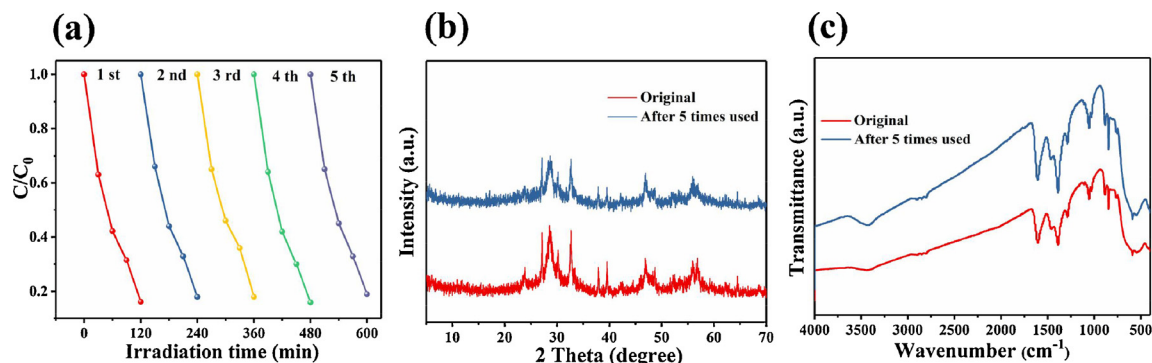
Fig. 8. (a) Photocatalytic recycle experiments for the 7% Bi/Bi$_3$NbO$_7$ sample. XRD patterns (b) and FTIR spectra (c) of original and used 7% Bi/Bi$_3$NbO$_7$ composites.
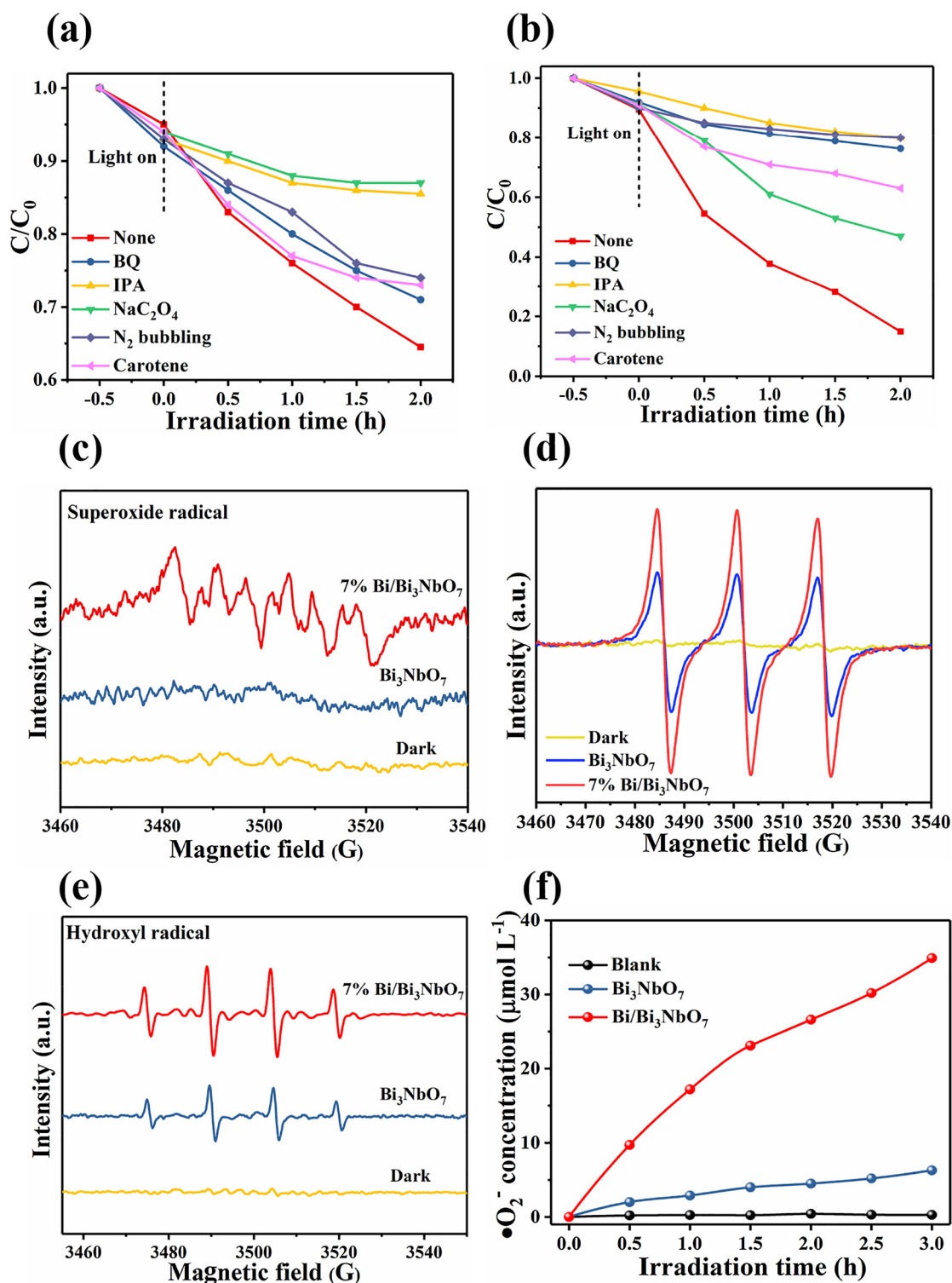
**Fig. 9.** Photocatalytic activities of (a) Bi_3NbO_7 and (b) 7% Bi/Bi_3NbO_7 composites for the CIP degradation with disparate scavengers; ESR spectra of the (c) DMPO-$\cdot O_2^-$, (d) DMPO-$^1O_2$ and (e) DMPO-$\cdot OH$ for Bi_3NbO_7 and the 7% Bi/Bi_3NbO_7 composite under visible light irradiation or in dark. (f) Quantitative determination of $\cdot O_2^-$'s generation for different samples.

composite displayed the powerful intensities as compared to Bi_3NbO_7. Meanwhile, singlet oxygen ($^1O_2$) was also detected by using TEMP as the trapping agents for $^1O_2$. From Fig. 9d, visible-light-irradiated Bi/Bi_3NbO_7 showed a boosted triplet signal which can be indexed to the signal of singlet oxygen ($^1O_2$) generation as compared with pristine Bi_3NbO_7 and Bi_3NbO_7 in dark [4]. As shown in Fig. 9e, the DMPO-$\cdot OH$ confirmed the 7% Bi/Bi_3NbO_7 exhibited the forceful intensities as

compared to Bi_3NbO_7, which reveals that more $\cdot OH$ were produced. The ESR spectra of $\cdot O_2^-$ and $^1O_2$ are in well consistent with the results of chemical trapping experiments. From the above discussion, it can be summarized that 0D/2D Bi/Bi_3NbO_7 composites could generate more $\cdot O_2^-$ and $^1O_2$ produced by molecular oxygen. For further understanding the molecular oxygen activation, NBT was chosen to quantify the $\cdot O_2^-$ concentration generated by Bi_3NbO_7 and Bi/Bi_3NbO_7
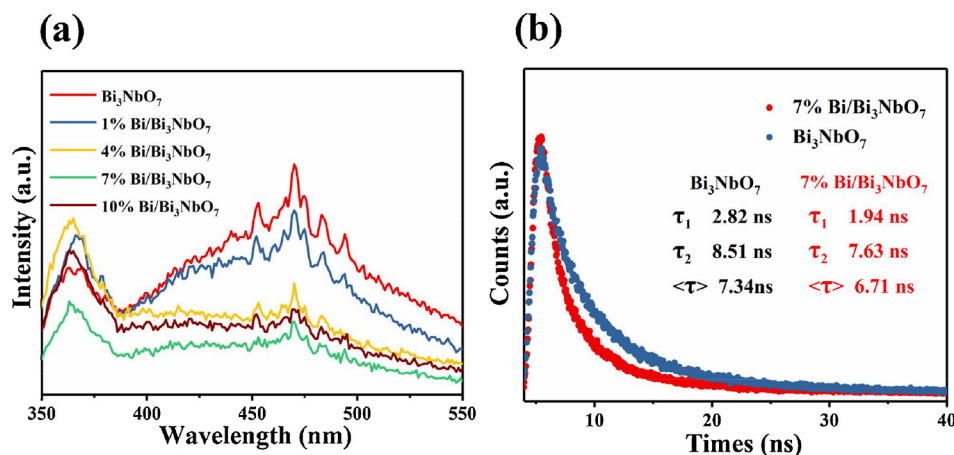
Fig. 10. (a) Photoluminescence spectroscopy of Bi_3NbO_7 and X% Bi/Bi_3NbO_7 (X = 1, 4, 7 and 10); (b) Time-resolved transient PL decay spectroscopy of Bi_3NbO_7 and 7% Bi/Bi_3NbO_7.

composite [4]. The concentration of $\cdot O_2^-$ produced with irradiation time can be determined, as shown in Fig. 9f. As expected, the Bi/Bi_3NbO_7 possesses a much higher $\cdot O_2^-$ concentration than that of Bi_3NbO_7 and blank one, which can be induced by its unique 0D/2D structure and faster interfacial charge transfer. It can be well confirmed that the Bi/Bi_3NbO_7 composites boosted the activation of molecular oxygen into $\cdot O_2^-$ species.

Photoluminescence emission spectroscopy (PL) and time-resolved transient PL decay spectra of samples were exhibited in Fig. 10 [44–47]. The relative weak PL intensity indicates a low recombination rate of the photoinduced carriers. Distinctly, the pure Bi_3NbO_7 and other X% Bi/Bi_3NbO_7 composites both show PL emission peak at 470 nm (compliance with the band gap of Bi_3NbO_7 from UV–vis diffuse reflectance results), but Bi/Bi_3NbO_7 samples display lower intensity than that of Bi_3NbO_7 (Fig. 10a). This phenomenon indicates that the recombination rate of photogenerated carriers was efficiently restrained through constructing the 0D/2D Bi/Bi_3NbO_7 composites, which is consistent with the result of photocatalytic degradation test. Photogenerated carriers' separation process was also studied by the time-resolved transient PL spectroscopy. The emission lifetimes of 7% Bi/Bi_3NbO_7 are shorter than the corresponding lifetimes of Bi_3NbO_7 nanosheets (short lifetime $\tau_1 = 1.94$ ns and long lifetime $\tau_2 = 7.63$ ns for 7% Bi/Bi_3NbO_7 versus short lifetime $\tau_1 = 2.82$ ns and long lifetime $\tau_2 = 8.51$ ns for Bi_3NbO_7). It is obvious that the τ value of Bi_3NbO_7 nanosheets is decreased from 7.34 ns to 6.71 ns after introducing the Bi nanodot. This observed shortening of emission lifetime reveals the emergence of the electronic interaction between 2D Bi_3NbO_7 nanosheets and 0D Bi nanodots [43]. What's more, the apparent electron transfer rate (k_{ET}) in 7% Bi/Bi_3NbO_7 composites can be calculated according to the equation:

$$k_{ET} = \frac{1}{\tau (7\% Bi/Bi_3NbO_7)} - \frac{1}{\tau (Bi_3NbO_7)}$$

The apparent electron transfer rate value is 1.61×10^7 s^{-1}, illustrating that the formed interface between 0D Bi nanodots and 2D Bi_3NbO_7 nanosheets is beneficial to the effective electron transfer quenching of the excitation state of Bi_3NbO_7 [20]. This fast electron-injection progress confirms that the 0D/2D structure remarkably accelerates charge transfer efficiency, thereby making for the molecular oxygen activation [46]. Both the lower PL intensity and the decreased fluorescence lifetime of Bi/Bi_3NbO_7 illustrated that the photogenerated carriers have been efficiently separated, which are superior to those of bare Bi_3NbO_7.

The transient photocurrent and electrochemical impedance spectroscopy (EIS) of the Bi_3NbO_7 and 7% Bi/Bi_3NbO_7 composite were exhibited in Fig. 11. The photocurrent density of 7% Bi/Bi_3NbO_7 (Fig. 11a) composite was much higher than those of Bi_3NbO_7, which

indicates that the Bi/Bi_3NbO_7 could lead to generating more charge carriers [48]. Generally, a smaller Nyquist curve indicated a flatter charge transfer resistance, which can be employed to study the dynamics of the localization state charges in the interface of the semiconductors. As shown in Fig. 11b, the sample 7% Bi/Bi_3NbO_7 possesses a smaller arc radius than Bi_3NbO_7, which reveals that the introduction of 0D Bi nanodots could shorten the recombination rate of photoinduced electron-hole pairs and dramatically enhance the photoelectrochemical performance of Bi/Bi_3NbO_7. Photoelectrochemical tests are in well consistent with the results of PL and time-resolved transient PL decay tests.

Based on the experimental results and the theory calculations above, a reasonable mechanism was presented in Scheme 2. The valance band spectrum of pure Bi_3NbO_7 was exhibited in Fig. S7. The electrons are excited from the valance band (VB) to the conduction band (CB) of Bi_3NbO_7 under visible light excitation, leaving the holes on the VB of Bi_3NbO_7 [21]. For pure Bi_3NbO_7, the conduction band were calculated to be -0.49 eV, which is much lower than the Fermi level of semimetal Bi nanodots (-0.17 eV). This relative potential refers to that the free electrons can easily transfer from Bi_3NbO_7 to semimetal Bi, which coincides with the previous study on interfacial electron transfer from the surface of semiconductor to the plasmonic metal [22,26]. Furthermore, the semimetal Bi nanodots can plays as a charge sink for continuously adopting the electrons induced from the CB of the Bi_3NbO_7 nanosheet. Meanwhile, the adsorbed molecule oxygen can trap these electrons to reduce to superoxide radical, and the holes left on the VB of Bi_3NbO_7 reacted with hydroxyl groups to generate hydroxyl radical, which are both crucial oxidants for photocatalytic antibiotics degradation [33,49]. Furthermore, sustainable singlet oxygen ($^1O_2$) generation could make by the process of charge transfer (that is, the direct oxidation of $\cdot O_2^-$ by holes), which means energy transfer is also a sustainable way for $^1O_2$ generation [42,49]. However, the photocatalytic activity of Bi/Bi_3NbO_7 is hampered when the semimetal Bi nanodots content is further increased. This phenomenon demonstrates that the excessive semimetal Bi nanoparticles on the surface of Bi_3NbO_7 nanostructures can block the active sites of Bi_3NbO_7 to generate carriers and this phenomenon has also been observed in other semiconductor/plasmonic metal system [50–52]. Meanwhile, the high surface area of photocatalysts can afford more adsorption sites for target pollutants [53]. Fig. S8 shows nitrogen adsorption-desorption isotherms of the pure Bi_3NbO_7 and 7% Bi/Bi_3NbO_7 sample. The specific surface areas of pure Bi_3NbO_7 and 7% Bi/Bi_3NbO_7 are 28.32 and 39.76 m^2/g, respectively. It can be observed that the higher specific surface areas in photocatalytic system also play a crucial part in the enhanced photocatalytic performance of the Bi/Bi_3NbO_7 composite. The formed 0D semimetal Bi nanodots/2D Bi_3NbO_7 nanosheets heterojunctions highly
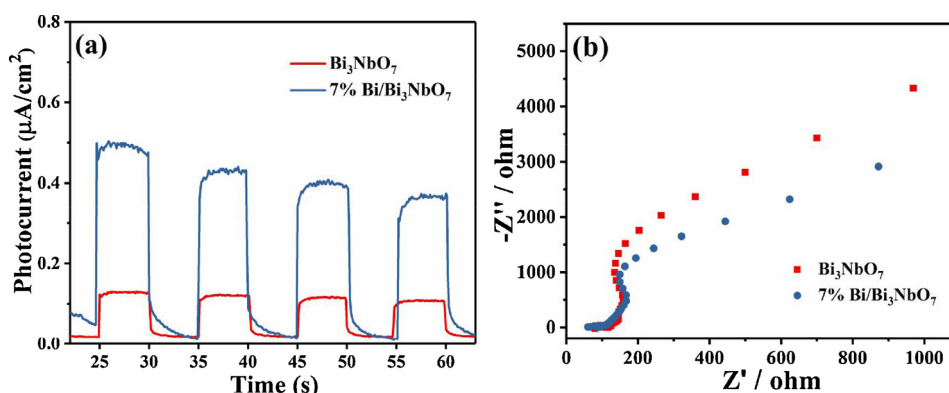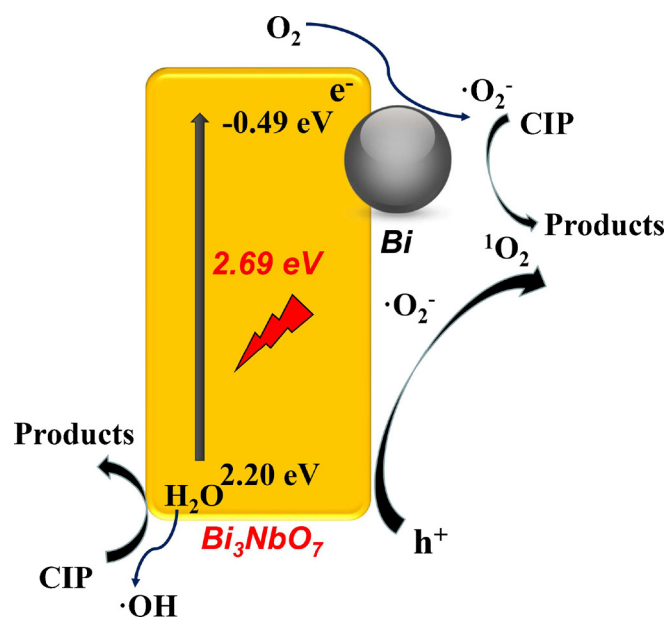
Fig. 11. (a) Transient photocurrent response and (b) Electrochemical impedance spectra of the Bi_3NbO_7 and 7% Bi/Bi_3NbO_7 under visible-light irradiation.

Scheme 2. Photocatalytic mechanism for Bi/Bi_3NbO_7 composite under visible light irradiation.

enhance the carriers' separation efficiency and further boost the molecular oxygen activation of the Bi/Bi_3NbO_7 composite [54]

4. Conclusions

A series of 0D/2D heterojunctions of Bi nanodot/Bi_3NbO_7 nanosheet are successfully synthesized through a simple two-step wet chemical method. The semimetal Bi nanodots are distributed uniformly on the surface of Bi_3NbO_7 nanosheets. A strong covalent interaction exists between the Bi atom of Bi nanodots and Bi−O layer on the surface of the Bi_3NbO_7 nanosheets, forming a charge transfer channel to transfer from Bi_3NbO_7 to metal Bi nanodots. The introduction of semimetal Bi increased the visible light absorption of the photocatalysts and significantly promoted molecular oxygen activation of Bi_3NbO_7 and improved the photocatalytic performance for degradation of CIP. The 0D/2D composite showed superior $\cdot O_2^-$ and $^1O_2$ generation as compared with pristine Bi_3NbO_7 under visible light irradiation. The photocatalytic degradation rate of ciprofloxacin (CIP) over the Bi/Bi_3NbO_7 composites is 4.58 times higher than that over the pristine Bi_3NbO_7. The composite still exhibited high stability and photocatalytic activity even after five cycles. This work not only understands the mechanism of the molecular oxygen activation in metal-semiconductor system, but also paves a way to design highly efficient 0D/2D photocatalysts for environmental remediation.

Appendix A. Supplementary data

Supplementary material related to this article can be found, in the online version, at doi: https://doi.org/10.1016/j.apcatb.2018.08.063.

References

[1] T. Chen, Q. Hao, W.J. Wang, C.L. Xie, D.M. Chen, C. Ma, W.Q. Yao, Y.F. Zhu, A honeycomb multilevel structure Bi_2O_3 with highly efficient catalytic activity driven by bias voltage and oxygen defect, Appl. Catal. B Environ. 237 (2018) 442–448.
[2] G.X. Yang, H.B. Yin, W.H. Liu, Y.P. Yang, Q. Zou, L.L. Lou, H.P. Li, Y.N. Huo, H.X. Li, Synergistic Ag/TiO_2-N photocatalytic system and its enhanced antibacterial activity towards *Acinetobacter baumannii*, Appl. Catal. B Environ. 224 (2018) 175–182.
[3] G.S. Li, Z.C. Lian, X. Li, Y.Y. Xu, W.C. Wang, D.Q. Zhang, F.H. Tian, H.X. Li, Ionothermal synthesis of black Ti^{3+}-doped single-crystal TiO_2 as an active photocatalyst for pollutant degradation and H_2 generation, J. Mater. Chem. A 3 (2015) 3748–3756.
[4] S.Y. Wang, X. Ding, X.H. Zhang, H. Pang, X. Hai, G.M. Zhan, W. Zhou, H. Song, L.Z. Zhang, H. Chen, J.H. Ye, In situ carbon homogeneous doping on ultrathin bismuth molybdate: a dual-purpose strategy for effcient molecular oxygen activation, Adv. Funct. Mater. (2017) 1703923.
[5] Y. Zheng, Z.H. Yu, H.H. Ou, A.M. Asiri, Y.L. Chen, X.C. Wang, Black phosphorus and polymeric carbon nitride heterostructure for photoinduced molecular oxygen activation, Adv. Funct. Mater. (2018) 1705407.
[6] J. Li, W.H. Zhao, J. Wang, S.X. Song, X.Y. Wu, G.K. Zhang, Noble metal-free modified ultrathin carbon nitride with promoted molecular oxygen activation for photocatalytic formaldehyde oxidization and DFT study, Appl. Surf. Sci. 458 (2018) 59–66.
[7] Y.F. Liu, W.Q. Yao, D. Liu, R.L. Zong, M. Zhang, X.G. Ma, Y.F. Zhu, Enhancement of visible light mineralization ability and photocatalytic activity of $BiPO_4/BiOI$, Appl. Catal. B Environ. 163 (2015) 547–553.
[8] J.J. Yang, D.M. Chen, Y. Zhu, Y.M. Zhang, Y. F. Zhu, 3D-3D porous Bi_2WO_6/graphene hydrogel composite with excellent synergistic effect of adsorption-enrichment and photocatalytic degradation, Appl. Catal. B Environ. 205 (2017) 228–237.
[9] H. Li, J. Shang, Z.H. Ai, L.Z. Zhang, Efficient visible light nitrogen fixation with BiOBr nanosheets of oxygen vacancies on the exposed {001} facets, J. Am. Chem. Soc. 137 (2015) 6393–6399.
[10] D.M. Chen, J.J. Yang, Y. Zhu, Y.M. Zhang, Y.F. Zhu, Fabrication of BiOI/graphene Hydrogel/FTO photoelectrode with 3D porous architecture for the enhanced photoelectrocatalytic performance, Appl. Catal. B Environ. 233 (2018) 202–212.
[11] H.F. Cheng, B.B. Huang, Y. Dai, Engineering BiOX (X = Cl, Br, I) nanostructures for highly efficient photocatalytic applications, Nanoscale 63 (2014) 2009–2026.
[12] J.G. Hou, Z. Wang, S.Q. Jiao, H.M. Zhu, Bi_2O_3 quantum-dot decorated nitrogen-doped Bi_3NbO_7 nanosheets: in situ synthesis and enhanced visible-light photocatalytic activity, CrystEngComm 14 (2012) 5923–5928.
[13] Y.M. Shen, Q.H. Wei, W.J. Guo, L.H. Fan, D.B. Liu, S.F. Li, Fabrication of Ag loaded Bi_3NbO_7 nanoparticles and its photocatalytic activity under visible light irradiation, J. Alloys Compd. 618 (2015) 311–317.
[14] H.H. Gan, G.K. Zhang, H.X. Huang, Enhanced visible-light-driven photocatalytic inactivation of Escherichia coli by $Bi_2O_2CO_3/Bi_3NbO_7$ composites, J. Hazard. Mater. 251 (2013) 131–137.
[15] G.K. Zhang, J.L. Yang, S.M. Zhang, Q. Xiong, B.B. Huang, J.T. Wang, W.Q. Gong,

Preparation of nanosized Bi$_3$NbO$_7$ and its visible-light photocatalytic property, J. Hazard. Mater. 172 (2009) 986–992.

[16] Q.Q. Wang, L.P. Yuan, M. Dun, X.M. Yang, H. Chen, J.L. Li, J.C. Hu, Synthesis and characterization of visible light responsive Bi$_3$NbO$_7$ porous nanosheets photocatalyst, Appl. Catal. B Environ. 196 (2016) 127–134.

[17] J. Li, J. Wang, G.K. Zhang, Y. Li, K. Wang, Enhanced molecular oxygen activation of Ni^{2+}-doped BiO$_{2-x}$ nanosheets under UV, visible and near-infrared irradiation: mechanism and DFT study, Appl. Catal. B Environ. 234 (2018) 167–177.

[18] K. Wang, X.Y. Wu, G.K. Zhang, J. Li, Y. Li, Ba$_5$Ta$_4$O$_{15}$ Nanosheet/AgVO$_3$ nanoribbon heterojunctions with enhanced photocatalytic oxidation performance: hole dominated charge transfer path and plasmonic effect insight, ACS Sustain. Chem. Eng. 6 (2018) 6682–6692.

[19] P. Wang, Y. Sheng, F.Z. Wang, H.G. Yu, Synergistic effect of electron-transfer mediator and interfacial catalytic active-site for the enhanced H$_2$-evolution performance: a case study of CdS-Au photocatalyst, Appl. Catal. B Environ. 220 (2018) 561–569.

[20] Z.W. Zhao, W.D. Zhang, Y.J. Sun, J.Y. Yu, Y.X. Zhang, H. Wang, F. Dong, Z.B. Wu, Bi Cocatalyst/Bi$_2$MoO$_6$ microspheres nanohybrid with SPR-promoted visible-light photocatalysis, J. Phys. Chem. C 120 (2016) 11889–11898.

[21] J.J. Wang, L. Tang, G.M. Zeng, Y.N. Liu, Y.Y. Zhou, Y.C. Deng, J.J. Wang, B. Peng, Plasmonic Bi metal deposition and g-C$_3$N$_4$ coating on Bi$_2$WO$_6$ microspheres for efficient visible-light photocatalysis, ACS Sustain. Chem. Eng. 5 (2017) 1062–1072.

[22] H.F. Cheng, K. Fuku, Y. Kuwahara, K. Moriab, H. Yamashita, Harnessing single-active plasmonic nanostructures for enhanced photocatalysis under visible light, J. Mater. Chem. A 3 (2015) 5244–5258.

[23] Z.Y. Wang, S. Yan, Y.J. Sun, T. Xiong, F. Dong, W. Zhang, Bi metal sphere/graphene oxide nanohybrids with enhanced direct plasmonic photocatalysis, Appl. Catal. B Environ. 214 (2017) 148–157.

[24] T. Xiong, X.G. Dong, H.W. Huang, W.L. Cen, Y.X. Zhang, F. Dong, Single precursor mediated-synthesis of Bi semimetal deposited N-Doped (BiO)$_2$CO$_3$ superstructures for highly promoted photocatalysis, ACS Sustain. Chem. Eng. 4 (2016) 2969–2979.

[25] P.P. Lei, R. An, P. Zhang, S. Yao, S.Y. Song, L.L. Dong, X. Xu, K.M. Du, J. Feng, H.J. Zhang, Ultrafast synthesis of ultrasmall Poly(Vinylpyrrolidone)-protected bismuth nanodots as a multifunctional theranostic agent for in vivo dual-modal CT/Photothermal-imaging-guided photothermal therapy, Adv. Funct. Mater. (2017) 1702018.

[26] H. Wang, W.D. Zhang, X.W. Li, J.Y. Li, W.L. Cen, Q.Y. Li, F. Dong, Highly enhanced visible light photocatalysis and in situ FT-IR studies on Bi metal@defective BiOCl hierarchical microspheres, Appl. Catal. B Environ. 225 (2018) 218–227.

[27] H. Wang, X.Z. Yuan, Y. Wu, G.M. Zeng, W.G. Tu, C. Sheng, Y.C. Deng, F. Chen, J. Wei Chew, Plasmonic Bi nanoparticles and BiOCl sheets as cocatalyst deposited on perovskite-type ZnSn(OH)$_6$ microparticle with facet-oriented polyhedron for improved visible-light-driven photocatalysis, Appl. Catal. B Environ. 209 (2017) 543–553.

[28] Z.B. Jiao, M.D. Shang, J.M. Liu, G.X. Lu, X.S. Wang, Y.P. Bi, The charge transfer mechanism of Bi modified TiO$_2$ nanotube arrays: TiO$_2$ serving as a "charge-transfer-bridge", Nano Energy 31 (2017) 96–104.

[29] S.B. Ning, H.X. Lin, Y.C. Tong, X.Y. Zhang, Q.Y. Lin, Y.Q. Zhang, J.L. Long, X.X. Wang, Dual couples Bi metal depositing and Ag@AgI islanding on BiOI 3D architectures for synergistic bactericidal mechanism of E. coli under visible light, Appl. Catal. B Environ. 204 (2017) 1–10.

[30] W.Q. Fan, C.F. Li, H.Y. Bai, Y.Y. Zhao, B.F. Luo, Y.J. Li, Y.L. Ge, W.D. Shi, H.P. Li, An in situ photoelectroreduction approach to fabricate Bi/BiOCl heterostructure photocathodes: understanding the role of Bi metal for solar water splitting, J. Mater. Chem. A 5 (2017) 4894–4903.

[31] S.X. Yu, Y.H. Zhang, M. Li, X. Du, H.W. Huang, Non-noble metal Bi deposition by utilizing Bi$_2$WO$_6$ as the self-sacrificing template for enhancing visible light photocatalytic activity, Appl. Surf. Sci. 391 (2017) 491–498.

[32] B. Wang, W.H. Feng, L.L. Zhang, Y. Zhang, X.Y. Huang, Z.B. Fang, P. Liu, In situ construction of a novel Bi/CdS nanocomposite with enhanced visible light photocatalytic performance, Appl. Catal. B Environ. 206 (2017) 510–519.

[33] Y.K. Huang, S.F. Kang, Y. Yang, H.F. Qin, Z.J. Ni, S.J. Yang, X. Li, Facile synthesis of Bi/Bi$_2$WO$_6$ nanocomposite with enhanced photocatalytic activity under visible light, Appl. Catal. B Environ. 196 (2016) 89–99.

[34] F. Dong, Q.Y. Li, Y.J. Sun, W.K. Ho, Noble metal-like behavior of plasmonic Bi

[35] X.W. Liu, H.Q. Cao, J.F. Yin, Generation and photocatalytic activities of Bi@Bi$_2$O$_3$ microspheres, Nano Res. 4 (2011) 470–482.

[36] X.D. Meng, G.K. Zhang, N. Li, Bi$_{24}$Ga$_2$O$_{39}$ for visible light photocatalytic reduction of Cr(VI): controlled synthesis, facet-dependent activity and DFT study, Chem. Eng. J. 314 (2017) 249–256.

[37] D.D. Tang, J. Li, G.K. Zhang, A novel open–framework spheniscidite photocatalyst with excellent visible light photocatalytic activity: silver sensitization effect and DFT study, Appl. Catal. B Environ. 224 (2018) 433–441.

[38] X.Y. Wu, X.Y. Wang, J. Li, G.K. Zhang, Boosting molecular oxygen activation of SrTiO$_3$ by engineering exposed facets for highly efficient photocatalytic oxidation, J. Mater. Chem. A 5 (2017) 23822–23830.

[39] K. Wang, G.K. Zhang, J. Li, Y. Li, X.Y. Wu, 0D/2D Z-Scheme heterojunctions of bismuth tantalate quantum dots/ultrathin g-C$_3$N$_4$ nanosheets for highly efficient visible light photocatalytic degradation of antibiotics, ACS Appl. Mater. Interfaces 9 (2017) 43704–43715.

[40] X.A. Dong, W.D. Zhang, Y.J. Sun, J.Y. Li, W.L. Cen, Z.H. Cui, H.W. Huang, F. Dong, Visible-light-induced charge transfer pathway and photocatalysis mechanism on Bi semimetal@defective BiOBr hierarchical microspheres, J. Catal. 357 (2018) 41–50.

[41] H.B. Yu, B.B. Huang, H. Wang, X.Z. Yuan, L.B. Jiang, Z.B. Wu, J. Zhang, G.M. Zeng, Facile construction of novel direct solid-state Z-scheme AgI/BiOBr photocatalysts for highly effective removal of ciprofloxacin under visible light exposure: mineralization efficiency and mechanisms, J. Colloid Interface Sci. 522 (2018) 82–94.

[42] X.J. Wen, C.G. Niu, L. Zhang, C. Liang, H. Guo, G.M. Zeng, Photocatalytic degradation of ciprofloxacin by a novel Z-scheme CeO$_2$-Ag/AgBr photocatalyst: Influencing factors, possible degradation pathways, and mechanism insight, J. Catal. 358 (2018) 141–154.

[43] X.Y. Zheng, S.P. Xu, Y. Wang, X. Sun, Y. Gao, B.Y. Gao, Enhanced degradation of ciprofloxacin by graphitized mesoporous carbon (GMC)-TiO$_2$ nanocomposite: strong synergy of adsorption-photocatalysis and antibiotics degradation mechanism, J. Colloid Interface Sci. 527 (2018) 202–213.

[44] Q. Hao, S.M. Hao, X.X. Niu, X. Li, D.M. Chen, H. Ding, Enhanced photochemical oxidation ability of carbon nitride by π–π stacking interactions with graphene, Chin. J. Catal. 38 (2017) 278–286.

[45] D.M. Chen, Z.H. Wang, T.Z. Ren, H. Ding, W.Q. Yao, R.L. Zong, Y.F. Zhu, Influence of defects on the photocatalytic activity of ZnO, J. Phys. Chem. C 118 (2014) 15300–15307.

[46] Y.X. Deng, M.Y. Xing, J.L. Zhang, An advanced TiO$_2$/Fe$_2$TiO$_5$/Fe$_2$O$_3$ triple-heterojunction with enhanced and stable visible-light-driven fenton reaction for the removal of organic pollutants, Appl. Catal. B Environ. 211 (2017) 157–166.

[47] W.L. Yu, J.X. Chen, T.T. Shang, L.F. Chen, L. Gu, T.Y. Peng, Direct Z-scheme g-C$_3$N$_4$/WO$_3$ photocatalyst with atomically defined junction for H$_2$ production, Appl. Catal. B Environ. 219 (2017) 693–704.

[48] G. Yang, D.M. Chen, H. Ding, J.J. Feng, J.Z. Zhang, Y.F. Zhu, S. Hamid, D.W. Bahnemann, Well-designed 3D ZnIn$_2$S$_4$ nanosheets/TiO$_2$ nanobelts as direct Z-scheme photocatalysts for CO$_2$ photoreduction into renewable hydrocarbon fuel with high efficiency, Appl. Catal. B Environ. 219 (2017) 611–618.

[49] Z.H. Wang, W.H. Ma, C. Chen, H.W. Ji, J.C. Zhao, Probing paramagnetic species in titania-based heterogeneous photocatalysis by electron spin resonance (ESR) spectroscopy-A mini review, Chem. Eng. J. 170 (2011) 353–362.

[50] H.G. Yu, W.J. Liu, X.F. Wang, F.Z. Wang, Promoting the interfacial H$_2$-evolution reaction of metallic Ag by Ag$_2$S cocatalyst: a case of TiO$_2$/Ag-Ag$_2$S photocatalyst, Appl. Catal. B Environ. 225 (2018) 415–423.

[51] H. Li, Z. Bian, J. Zhu, Y. Huo, Y. Lu, Mesoporous Au/TiO2 nanocomposites with enhanced photocatalytic activity, J. Am. Chem. Soc. 129 (2007) 4538–4539.

[52] Z. Wang, C.L. Jiang, R. Huang, H. Peng, X.D. Tang, Investigation of optical and photocatalytic properties of bismuth nanospheres prepared by a facile thermolysis method, J. Phys. Chem. C 118 (2014) 1155–1160.

[53] D. Du, W. Shi, L.Z. Wang, J.L. Zhang, Yolk-shell structured Fe$_3$O$_4$@void@TiO$_2$ as a photo-Fenton-like catalyst for the extremely efficient elimination of tetracycline, Appl. Catal. B Environ. 200 (2017) 484–492.

[54] J. Li, X.Y. Wu, W.F. Pan, G.K. Zhang, Chen H, Vacancy-rich monolayer BiO$_{2-x}$ as highly efficient UV, Visible and Near-Infrared responsive photocatalyst, Angew. Chem. Int. Ed. 57 (2018) 491–495.